A parametric study of LEM3D based on comparison with a turbulent lifted hydrogen jet flame in a vitiated co-flow

Fredrik Grøvdal[a,*], Sigurd Sannan[b], Jyh-Yuan Chen[c], Terese Løvås[a]

[a] *NTNU, Department of Energy and Process Engineering, NO-7034 Trondheim, Norway*
[b] *SINTEF Energy Research, NO-7465 Trondheim, Norway*
[c] *Department of Mechanical Engineering, University of California - Berkeley, Berkeley, CA 94720, USA*

Abstract

A novel model, the hybrid RANS-LEM3D model, is applied to a lifted turbulent N_2 diluted hydrogen jet flame in a vitiated co-flow of hot products from lean H_2/air combustion. In the present modeling approach, mean-flow information from RANS provides model input to LEM3D, which returns the scalar statistics needed for more accurate mixing and reaction calculations. The dependence of lift-off heights and flame structure on iteration schemes and model parameters are investigated in detail, along with other characteristics not available from RANS alone, such as the instantaneous and detailed species profiles and small-scale mixing. Two different iteration procedures, a breadth-first search and a checkerboard algorithm, as well as parameters of the model framework are examined and tested for sensitivity towards the results. The impact of heat release and thermal expansion is demonstrated and evaluated in detail. It is shown for the current application that LEM3D provides additional details compared to the RANS simulation with a low computational cost in comparison to a conventional DNS simulation.

Keywords: Turbulent mixing, Linear Eddy Model, Vitiated Co-flow Burner, Kolmogorov scale, Differential diffusion, 3×1D solver

1. Introduction

In the successful design of combustors, e.g., the development of novel gas turbine combustors, the use of numerical simulation tools that are able to give accurate predictions of the combustion physics and kinetics is crucial in order to increase efficiency and reduce emissions. However, state-of-the-art simulation tools, based on the Reynolds Averaged Navier-Stokes (RANS) equations, have limited predictive capabilities in many practical engineering applications. This is due to the lack of spatial and temporal resolution in conventional RANS methods. The most accurate method for studying turbulent reacting flows numerically is by Direct Numerical Simulation (DNS), in which the Navier-Stokes equations are solved directly without any turbulence model (Hawkes et al., 2005). Since the computational cost is extremely large, however, DNS for a complete combustor geometry is beyond reach even with the most powerful computers of today.

*Corresponding author.
Email address: fredrik.grovdal@ntnu.no (Fredrik Grøvdal)

This is the accepted version of an article published in Combustion Science and Technology
http://dx.doi.org/10.1080/00102202.2019.1588261

A compromise made by conventional models is that they do not explicitly separate molecular mixing and turbulent stirring as distinct processes at the subgrid level. Thus, turbulent stirring, which by nature is advective, is treated as a diffusion process and the dissimilar influences of these mechanisms are smeared out. This is the case both for RANS methods and Large Eddy Simulation (LES). In combustion, the explicit distinction between turbulent stirring, diffusive mixing, and chemical reaction at all scales is critical to the overall ability to capture phenomena such as ignition, extinction, unmixedness, and turbulent flame speed, etc. To capture the principal mechanisms governing turbulent stirring and diffusive mixing, Kerstein (1988, 1991) formulated the Linear Eddy Model (LEM), which was then extended to include chemical reactions (Kerstein, 1992). The One-Dimensional Turbulence (ODT) model, also developed by Kerstein (1999), subsumes the capabilities of LEM with regard to mixing and evolves velocity fields in addition to scalar profiles. Both LEM and ODT are one-dimensional models that resolve all scales of turbulent reactive flows at a computationally affordable cost.

Applications of the standalone 1D LEM have been limited to relatively simple flow configurations, such as flows that are homogeneous in at least one spatial direction (McMurtry et al., 1993a). For more complex flows, the approach has been to couple the model to global flow solvers. McMurthy et al. (1992); McMurtry et al. (1993b) proposed to use LEM as a subgrid mixing and chemistry closure for LES. In this modeling approach, the unresolved length and time scales of LES are captured by individual LEM domains associated with each LES control volume. The LEM domains communicate with each other by means of a splicing procedure. The mass transfer across each LES mesh face during the LES time step is computed based on the LES-resolved mass fluxes. By the splicing mechanism, the prescribed transfer is applied to the affected LEM domains by cutting an end portion of the upwind domain of the LES face and pasting it onto one of the two endpoints of the downwind domain of the LES face. The complete LEMLES model, with two-way coupling between LEM and LES, was later demonstrated for scalar mixing and non-premixed combustion by Menon and Calhoon Jr (1996). The LEMLES model has also been applied to premixed combustion with promising results (Chakravarthy and Menon, 2000; Sankaran and Menon, 2005; Sen and Menon, 2010). In a more recent development, Ranjan et al. (2016) has proposed an alternative subgrid closure to LEMLES in which the splicing is discarded and the large-scale molecular diffusion is included in a manner similar to the conventional LES. This approach leads to improved predictions of the flame structure of premixed flames under given conditions but has the disadvantage that it cannot capture counter-gradient turbulent transport.

The standalone ODT model has been shown to accurately reproduce DNS data for a nonpremixed turbulent jet flame (Punati et al., 2011). The use of ODT as a subgrid model for LES was first suggested and described by Kerstein (2002). In the ODTLES model, three mutually orthogonal arrays of one-dimensional domains are embedded within the coarser LES mesh (Schmidt et al., 2010). The approach allows for the large-scale turbulent motions to be captured by the LES part of the model, while the small-scale processes are resolved by the ODT along a network of intersecting 1D lines throughout the system. Both LEMLES

This is the accepted version of an article published in Combustion Science and Technology
http://dx.doi.org/10.1080/00102202.2019.1588261

and ODTLES represent promising modeling approaches that resolve the turbulence-chemistry interactions at the smallest scales of turbulent reactive flows at a computationally affordable cost compared to DNS.

In this paper we investigate a hybrid model in which a 3-dimensional formulation of the Linear Eddy Model (LEM3D) is used as a post-processing tool for an initial RANS simulation. The use of LEM coupled to RANS has been proposed previously, but to date there has been limited demonstration and evaluation of this approach for combustion applications (Goldin et al., 1995). The LEM3D approach has been developed by Sannan et al. (2013) and is formulated to provide small-scale resolution in all three spatial directions of a turbulent flow field. The formulation incorporates three orthogonally intersecting arrays of 1D LEM domains, with intersecting LEM domains coupled in a Lagrangian sense by non-diffusive fluid-cell displacements. Thus, thermodynamical quantities are advected with no numerical transport, thereby maintaining the strict segregation of advective and molecular diffusive time advancement that provides maximum fidelity for combustion applications. For the work presented here, LEM3D is coupled to the state-of-the-art flow solver ANSYS Fluent, and the coupled RANS-LEM3D tool has the potential of direct industrial application with allowance for complex geometries such as in gas turbine combustors.

In the hybrid RANS-LEM3D approach, LEM3D complements RANS with unsteadiness and small-scale resolution in a computationally efficient manner. The hybrid model is broadly analogous to LEMLES in its physical treatment, but differs in its overall structure in ways that facilitate its future use as a flexible tool for mixing and chemical reaction simulation within 3D flow solutions. Thus, the three-array substructure of LEM domains in LEM3D has the potential of accommodating direction-dependent physics such as buoyancy and flame quenching near a wall. The spatial structure of LEM3D is incidentally the same as in ODTLES, but the domain coupling of LEM3D is expressly designed to avoid numerical transport and its consequences. In the present study, we employ the hybrid RANS-LEM3D model with detailed chemistry to investigate the stabilization mechanism and flame structure of a turbulent lifted hydrogen jet flame in a vitiated co-flow.

The vitiated co-flow burner, used for comparison in the present study, was developed at UC Berkeley and first presented by Cabra et al. (2002); see also Cabra (2003). The co-flow burner enables studies of flame lift-off and stabilization mechanisms in an environment similar to that of a gas turbine combustor. In practical applications, the lifting of the flame base off the burner has the advantage both of avoiding thermal contact between the flame and the pilot nozzle, which would lead to erosion of the burner material, and potential flashbacks, in particular for hydrogen enriched fuels. The disadvantage of the flame stabilization technique is that the lifted flame blows off more easily than attached flames and therefore must be continuously controlled.

The role of autoignition in the stabilization and appurtenant lift-off heights of turbulent H_2/N_2 flames issuing into hot co-flows of combustion products has been extensively studied by, e.g., Masri et al. (2004) and Cao et al. (2005) using PDF calculations. Myhrvold et al. (2006) conducted a series of simulations and indicated the extent to which turbulence models influence the predicted lift-off height using the Eddy Dissipation Concept by Magnussen (1981, 1989). The study of Cao et al. (2005) indicates that the lift-off is primarily controlled by chemistry. However, autoignition events in unsteady flames have been shown to

This is the accepted version of an article published in Combustion Science and Technology
http://dx.doi.org/10.1080/00102202.2019.1588261

be controlled by both chemistry and turbulent mixing (Johannessen et al., 2015). The discussion on flame stabilization on the vitiated burner set-ups seemed to be put to an end with the 3D DNS study of a planar hydrogen jet at Sandia National Laboratories by Yoo et al. (2009). In this configuration, with the hydrogen jet issuing with high velocity into hot slow air, the authors concluded that autoignition is the key mechanism responsible for flame stabilization of the lifted flame. These findings were later confirmed in the review article by Mastorakos (2009) on ignition of turbulent non-premixed flames.

This paper aims to give further insight into the sensitivity of the hybrid RANS-LEM3D model to adjustable parameters to demonstrate the strengths of the model but also to point towards issues that require special attention. In Section 2, the LEM3D model is explained in depth. A new iteration scheme previously not used for LEM3D, based on the breadth-first search (BFS) invented by Zuse (1972), is introduced in sub-section 2.4. The coupling of the LEM3D mixing and reaction model to the computational fluid dynamics (CFD) flow solver is established in sub-section 2.6. Parameter and iteration sensitivities are discussed in Section 3 and applied to the vitiated co-flow burner, and the final conclusions are contained in Section 4.

2. Numerical Model and Setup

2.1. The Linear Eddy Model

The Linear Eddy Model is formulated to explicitly distinguish between the effects of turbulent stirring, molecular diffusion, and chemical reaction in a turbulent reactive flow (Kerstein, 1988, 1991, 1992). This is achieved by a reduced description of the scalar fields in one dimension, which makes a full-scale resolution of all spatial and temporal scales, down to the smallest turbulence scales, computationally feasible. The governing transport equation for chemical species k can be written as

$$\frac{\partial \rho Y_k}{\partial t} = \frac{\partial}{\partial x}\left[\rho D_k \frac{\partial Y_k}{\partial x}\right] + TM + \rho\omega_k, \tag{1}$$

where ρ is the density, Y_k is the k-th species mass fraction, D_k is the molecular diffusivity, and $\rho\omega_k$ is the chemical reaction source term. Similarly, the transport equation for the specific enthalpy h is written as

$$\frac{\partial \rho h}{\partial t} = \frac{\partial}{\partial x}\left[\rho \kappa \frac{\partial h}{\partial x}\right] + TM + S_h, \tag{2}$$

where κ is the thermal conductivity, and S_h is the heat source term due to chemical reaction. The term TM in the above equations symbolically denotes randomly occurring stirring events (triplet maps) that punctuate the diffusion and chemical reaction processes.

The triplet maps are stochastic events in LEM that emulate the effects of turbulent eddies on the scalar concentration fields. In Lagrangian terminology, the triplet maps rearrange fluid cells, represented by the computational cells of the discretized one-dimensional domain, in such a manner that scalar lengths are reduced and local gradients are magnified. This is in accordance with the effects of compressive strain in turbulent flow, as illustrated in Figure 1. The left-hand-side of the figure shows an iso-distribution in space of a scalar ϕ and its amplitude along a 1D line of sight at a time t_0. The right-hand-side of the figure illustrates

This is the accepted version of an article published in Combustion Science and Technology
http://dx.doi.org/10.1080/00102202.2019.1588261

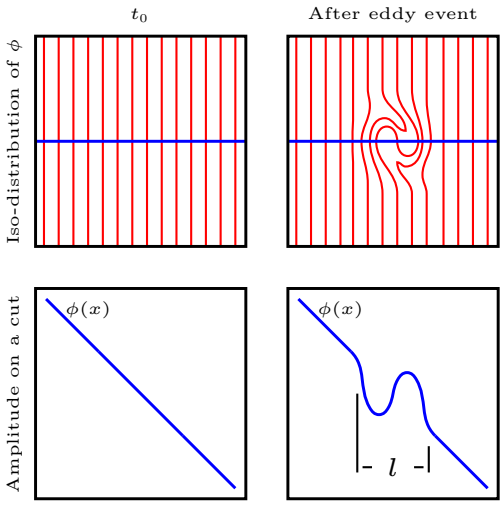

Figure 1: Schematic illustration of the effect of a turbulent eddy of size l on a distribution ϕ in space and the amplitude $\phi(x)$ along a 1D line of sight.

the effect of a turbulent eddy together with molecular diffusion on the iso-contours and the amplitude $\phi(x)$ along the line of sight. In physical flow, molecular diffusion and turbulent eddies are continuous processes. In LEM, the eddy events are instantaneous maps sampled from an inertial range size distribution followed by molecular diffusion and eventual chemical reactions in the case of reactive flows.

The turbulent stirring implied by the triplet maps represents turbulent advection and is a distinct physical mechanism governing the mixing of scalar fields. In conventional CFD approaches, such as RANS, turbulent mixing is treated as a diffusion term through the mass-averaged scalar flux $\overline{\rho}\,\widetilde{u_j''\,\phi''} = -\overline{\rho} D_T \frac{\partial \widetilde{\phi}}{\partial x_j}$, where $\overline{\rho}$ denotes the mean of ρ, $\phi'' = \phi - \widetilde{\phi}$ is the fluctuation of ϕ about the Favre-averaged $\widetilde{\phi} = \overline{\rho\phi}/\overline{\rho}$, u_j'' is the fluctuation of the velocity component u_j about the Favre-averaged $\widetilde{u}_j$, and D_T is the turbulent diffusivity. This is called the gradient-diffusion assumption where D_T is positive. The implication is that the scalar flux is in the opposite direction of the mean scalar gradient vector, i.e., the transport of a scalar is always in the direction from a region of high mean concentration to a region of lower concentration. For inhomogeneous, anisotropic turbulence, however, this might not be the case. In such regions counter-gradient diffusion may occur which does not obey the gradient-diffusion assumption. In LEM, the turbulent diffusivity D_T gives the rate of stirring events.

The molecular diffusion $\frac{\partial}{\partial x}\left(\rho D_k \frac{\partial Y_k}{\partial x}\right)$ and chemical reactions $\rho\omega_k$ of Eq. (1), together with the thermal conduction $\frac{\partial}{\partial x}\left(\rho\,\kappa\,\frac{\partial h}{\partial x}\right)$ and heat source S_h of Eq. (2), are solved directly on the LEM domain. The reactive-diffusive processes are punctuated by the stochastic triplet map events TM. Hence, the stochastic stirring and mixing processes affect the chemical reactions, and the subsequent heat release and dilatation exhibit random behavior.

This is the accepted version of an article published in Combustion Science and Technology
http://dx.doi.org/10.1080/00102202.2019.1588261

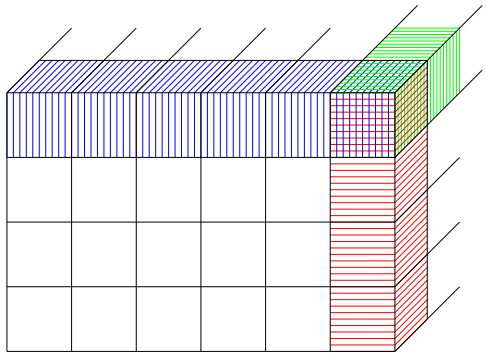

Figure 2: The flow domain of the LEM3D simulation with the coarse Cartesian mesh. The superimposed fine-scale resolution is illustrated by the coloured LEM domains in red, blue and green. One domain is shown in each direction and these intersect in the top-front corner control volume, 3DCV, of the LEM3D domain. Note that the actual LEM resolutions used in the simulations are much higher than shown in the figure.

2.2. LEM3D

The LEM3D formulation, described in detail by Weydahl (2010) and Sannan et al. (2013), incorporates three orthogonally intersecting arrays of 1D LEM domains, with intersecting LEM domains coupled in a Lagrangian sense by non-diffusive fluid-cell transfers from one domain to another. LEM3D thus provides small-scale resolution in all three spatial directions of the turbulent flow field, as well as time-resolved unsteadiness. As in 1D LEM, LEM3D involves stochastic rearrangement events of fluid cells, but is extended to include transfers of fluid cells between the LEM domains. Thereby, LEM3D maintains the explicit distinction of advective and molecular diffusive time advancements which is critical to a high fidelity for combustion applications.

The governing transport equations follow the structure of the 1D LEM, but include respective advection terms $\partial(\overline{\rho u_\alpha} Y_k)/\partial x_\alpha$ and $\partial(\overline{\rho u_\alpha} h)/\partial x_\alpha$, i.e.,

$$\frac{\partial \rho Y_k}{\partial t} + \frac{\partial \overline{\rho u_\alpha} Y_k}{\partial x_\alpha} = \frac{\partial}{\partial x_j}\left[\rho D_k \frac{\partial Y_k}{\partial x_j}\right] + TM_j + \rho\omega_k, \tag{3}$$

$$\frac{\partial \rho h}{\partial t} + \frac{\partial \overline{\rho u_\alpha} h}{\partial x_\alpha} = \frac{\partial}{\partial x_j}\left[\rho \kappa \frac{\partial h}{\partial x_j}\right] + TM_j + S_h, \tag{4}$$

where the index j indicates that the terms are implemented on 1D domains in all three spatial directions. Here, TM_j denotes triplet maps occurring on a particular 1D domain. Note that the conventional summation over repeated indices does not apply to the right hand side of the equation.

Reactive-diffusive time advancement takes place on each LEM domain in small sub-cycling steps within a coarser time step. The sub-cycling is punctuated by the stochastically occurring stirring events, i.e., the triplet maps. The rate of triplet maps is determined by the turbulent diffusivity D_T which is an input to the model. In domains where $D_T \approx 0$, i.e. in the laminar limit, there is no triplet map activity and the reactive-diffusive processes are time advanced with no punctuations within the coarser time step.

This is the accepted version of an article published in Combustion Science and Technology
http://dx.doi.org/10.1080/00102202.2019.1588261

The coupling of the intersecting LEM domains is associated with the advection terms and the larger time step corresponding to the coarse-grained spatial scale defined by the intersections of orthogonal LEM domains (see sub-section 2.4 for a comprehensive discussion). By construction, these intersections define a Cartesian mesh of cubic control volumes (3DCVs), as shown in Figure 2. Each of the 3DCVs are resolved in all three spatial directions by an equal number of LEM cells. The advection process $\partial(\overline{\rho u_\alpha}\phi)/\partial x_\alpha$ for $\phi = \{Y_k, h\}$ is governed by an averaged mass flux $\overline{\rho \boldsymbol{u}}$ which may be prescribed from a global flow solver or measurements. The advection is implemented deterministically by Lagrangian displacements of fluid cells.

The remaining terms of Eqs. (3) and (4) are explained in sub-section 2.1. Note, however, that the heat release and thermal expansion due to the source terms $\rho\,\omega_k$ and S_h impact the advection process and the coupling of the intersecting LEM domains. The source terms are here solved directly by the use of the stiff solver DVODE (Brown et al., 1989).

The model input to LEM3D includes mean-flow information such as the mass flux $\overline{\rho \boldsymbol{u}}$ and the turbulent diffusivity field D_T for the turbulent field. While the mass flux governs the advective transport of scalars, the turbulent diffusivity governs the turbulent stirring by providing the rate at which turbulent eddy events occur. Both the mass flux $\overline{\rho \boldsymbol{u}}$ and the turbulent diffusivity D_T typically vary in the spatial directions and are resolved at the coarser length scale only, corresponding to the 3DCVs. The mean-flow information is here obtained from an initial RANS simulation, with the values of D_T fed to the centers of the 3DCVs and the face-normal components of $\overline{\rho \boldsymbol{u}}$ provided to the 3DCV faces. Other model inputs to LEM3D include local values, also fed to the 3DCV centers, of the integral length scale L_{int} and the Kolmogorov scale η. A more detailed discussion of the LEM3D model input and the coupling to RANS is contained in sub-section 2.6.

2.3. Implementation of chemistry

The LEM3D model may be viewed as a '1D-DNS' in all three directions, i.e., all relevant length scales are resolved down to the Kolmogorov scale, or down to the Batchelor scale as needed in case this is smaller than the Kolmogorov scale. Hence, the 1D LEM cells, also called LEM wafers, may be considered as homogeneous reactors with the chemistry implemented directly without any modeling. Thermal expansion, i.e. dilatation, is accounted for by increasing the wafer volume and performing a regridding subsequent to every diffusive-reactive time step.

Differential diffusion effects have been recognized for a long time to have a significant impact on turbulent hydrogen-rich flames (Bilger, 1982; Moo Lee and Dong Shin, 1988; Bisetti et al., 2009). The molecular diffusivity of the k-th chemical species is here represented by the mixture-averaged diffusion coefficient D_k (Bird et al., 1960). Hence, the model accommodates the effects of differential diffusion, as shown in previous studies by Sannan and Kerstein (2014, 2016).

In the current formulation, detailed and finite-rate chemistry is fully implemented from CHEMKIN II. The implicit, backward Euler time integration is employed, where the diffusion time step is given by the linear stability condition $\Delta t_D = \Delta x_w^2/D_{max}$ when Δx_w denotes the LEM wafer size. Here, $D_{max} = \max(D_{k,l})$,

This is the accepted version of an article published in Combustion Science and Technology
http://dx.doi.org/10.1080/00102202.2019.1588261

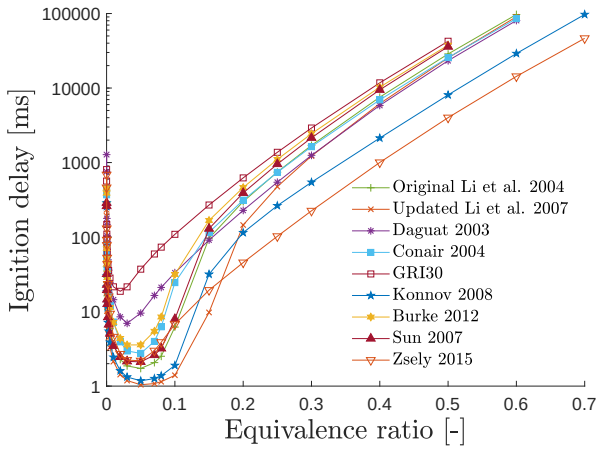

Figure 3: Ignition delay times vs. equivalence ratio for different mechanisms. The inlet conditions for the vitiated co-flow burner were used for this comparison, i.e., co-flow with $T = 1045$K, $Y_{H_2O} = 0.0989$, $Y_{N_2} = 0.7532$ and $Y_{O_2} = 0.1474$.

where $D_{k,l}$ is the mixture-averaged diffusion coefficient of species k at the l-th cell location of a given LEM domain. For very stiff chemistry, the characteristic chemical time scale associated with the reaction rate may be smaller than the diffusion time scale which could lead to inaccuracies. In this case, the value of D_{max} should be reduced accordingly.

The chemical reaction mechanism employed in the current study is the detailed H_2/O_2 mechanism of Li et al. (2004). The use of the Li mechanism is here chosen from a comparison of ignition delay times of several kinetic schemes with the inlet conditions of the Cabra vitiated co-flow burner, computed with a UC Berkeley in-house code and shown in Figure 3. The investigated mechanisms by Li et al. (2004, 2007); Dagaut et al. (2003); Ó Conaire et al. (2004); Smith et al. (1999); Konnov (2008); Burke et al. (2012); Sun et al. (2007); Zsély et al. (2005) were selected among all major mechanisms published after 1999, and hence among the most widely used mechanisms in hydrogen combustion (Olm et al., 2014). The Li mechanism compares well to most of the other mechanisms, and there are no extremes along the ignition delay curve.

A study looking into detailed reaction mechanisms for hydrogen combustion under gas turbine conditions was done by Ströhle and Myhrvold (2007). The investigation showed that the Li mechanism accurately represents H_2/O_2 chemical kinetics at elevated pressures, as present in a typical gas turbine combustor. The Li mechanism has previously also been used in a similar configuration to the Cabra burner, e.g., Yoo et al. (2007) conducted a three dimensional DNS simulation of a turbulent lifted hydrogen/air jet flame in a heated co-flow.

2.4. Domain couplings

The benefit of LEM3D compared to a DNS, namely the computational speed-up, introduces by construction the artifact of solving a 3D-dimensional flow configuration through arrays of coupled 1D domains. The coupling of the LEM domains is hence a crucial part of the model. As discussed by Sannan et al. (2013), the coupling is associated with the advective time step Δt and consists of two operations:

This is the accepted version of an article published in Combustion Science and Technology
http://dx.doi.org/10.1080/00102202.2019.1588261

1. Advective coupling provided by the term $\partial(\overline{\rho u_\alpha}\phi)/\partial x_\alpha$, where $\phi = Y_k$ for Eq. (3) and $\phi = h$ for Eq. (4). The displacement of LEM wafers are based upon the prescribed mass fluxes $\overline{\rho \boldsymbol{u}}$ given from RANS, while accounting for dilatations from reactions due to the source terms $\rho\,\omega_k$ and S_h. Typically, this involves transfers of wafers among the differently oriented LEM domains intersecting each 3DCV. Conservation of volume is enforced by requiring the displacements of wafers in and out of each 3DCV to obey the equation

$$\sum_{l=1}^{N_{\text{faces}}} \delta_l = 0, \tag{5}$$

where $N_{\text{faces}} = 6$ and δ_l denotes the integer number of wafer displacements across the 3DCV faces. A 2D illustration of the advection operation is shown in Figure 4.

2. An auxiliary coupling is implemented by stochastic rotations of the 3DCVs. The rotations give additional fluid exchanges between the LEM domains, and ensure that physical processes are consistently represented in all spatial directions. Thus, for every advective time step the 3DCVs are rotated $\pm 90°$ about any of the three coordinate axes with a locally defined probability

$$p_{\text{rot}} = \frac{3}{2} C_{\text{rot}} \cdot \text{CFL}_{\text{3DCV}}, \tag{6}$$

where CFL_{3DCV} is the local Courant-Friedrichs-Lewy number, and C_{rot} is a model constant. The effects of varying C_{rot} are investigated in Section 3. Note that p_{rot} might exceed 1 in the above expression for large C_{rot}, but that the restriction $p_{\text{rot}} \leq 1$ is implemented in the code. Since the rotations introduce diffusive transport, the induced diffusivity D_T^{rot} is deducted from the turbulent diffusivity such that the remaining triplet map diffusivity D_T^{TM} is given by

$$D_T^{TM} = D_T - D_T^{\text{rot}} = D_T - \frac{3}{4}\frac{V_{\text{3DCV}}}{\Delta x}\left\langle \delta^2 \right\rangle. \tag{7}$$

Here, V_{3DCV} is the absolute value of the largest velocity component associated with the 3DCV faces, Δx is the RANS mesh size, and $\left\langle \delta^2 \right\rangle$ denotes the mean-square single rotation displacement of the wafers in the 3DCV in the directions orthogonal to the rotational axis.

The advection operation follows the procedure described by Sannan et al. (2013), where the displacements of LEM wafers across the 3DCV interfaces are determined layer by layer, starting with the upstream first layer of 3DCVs of the computational domain. Integer wafer displacements across the 3DCV interfaces are enforced by a round-off management scheme which introduces residuals between the integer-based and the prescribed mass fluxes across the interfaces. Thus, the residual associated with face l of a 3DCV is given by

$$\Xi_l = \Delta x_w \sum_{j=1}^{N_l} \rho_{lj} - \overline{\rho\, u}_l\, \Delta t, \tag{8}$$

where N_l is the number of wafers to be fluxed over face l, ρ_{lj} denotes the density of wafer j to be fluxed into or out of the 3DCV at face l, and $\overline{u_l}$ is the fixed RANS velocity at face l. The instantaneous LEM3D velocity

This is the accepted version of an article published in Combustion Science and Technology
http://dx.doi.org/10.1080/00102202.2019.1588261

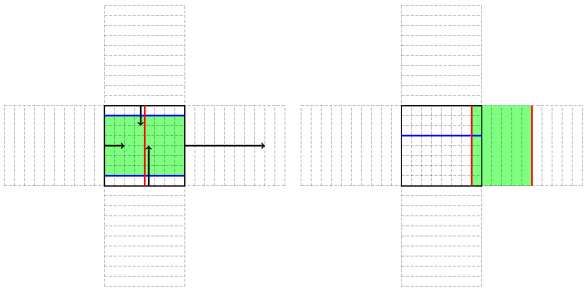

Figure 4: A 2D illustration of the advection operation associated with a given 3DCV. The arrows in the left figure indicate the given wafer displacements in the donor domain (vertical) and the receiver domain (horizontal), with the resulting displacements shown in the figure to the right. The six excess wafers (in green) in the donor are extracted from the center of the 3DCV, rotated counter-clockwise or clockwise (randomly chosen), and then displaced and inserted into the receiver so as to fill the gap created by the advection of that domain. The wafer displacements in the donor correspondingly fill the gap left by the extracted wafers.

v_l associated with the flux $\Delta x_w \sum_{j=1}^{N_l} \rho_{lj}$ is $v_l = \overline{u}_l + u'_l$, where u'_l is the time-dependent velocity implied by the residual Ξ_l.

Due to the increase of volume through heat release from reactions, following the ideal gas law for constant pressure, large deviations from the prescribed mass fluxes may occasionally occur. In order to minimize these deviations, an investigation of various iteration procedures, in combination with a least-squares method to minimize the residuals (8) at each 3DCV face, has been performed. In these procedures, the sum of squared deviations

$$d2 = \sum_{l=2}^{N_{\text{faces}}} \left(\Xi_l + \text{sgn}(\Delta_l) \Delta x_w \sum_{n=\text{sgn}(\Delta_l)}^{\Delta_l} \rho_{ln} \right)^2 , \tag{9}$$

is minimized for each 3DCV (subject to a constraint), where the sum is over the lateral ($l = 2, \ldots, 5$) faces and the downstream face ($l = 6$) of the 3DCV. The mass flux across the upstream face ($l = 1$) of the 3DCV is not part of the above sum since this is already determined from the flux calculated for the 3DCV immediately upstream, or from the upstream boundary conditions in the case of the first layer of 3DCVs. The quantities Δ_l are integer corrections to the preliminary assigned wafer displacements, determined by minimizing $d2$ and subject to the constraint $\sum_{l=2}^{N_{\text{faces}}} \Delta_l = 0$ to preserve the volume. In addition, the continuity equation is built into the formulation and applied at every advective time step Δt.

Even though the residuals Ξ_l are minimized through the least-squares method, there is an associated total deviation Ξ_{flux} for each 3DCV between the actual integer-based and prescribed mass fluxes given by

$$\Xi_{\text{flux}} = \sum_{l=1}^{N_{\text{faces}}} \Xi_l . \tag{10}$$

The deviation Ξ_{flux} is an integral part of the current implementation in the variable density framework and in the presence of chemical reactions. In the original implementation for constant-density applications (Sannan et al., 2013), a checkerboard algorithm was employed to minimize the residuals Ξ_l. Here, a breadth-first

This is the accepted version of an article published in Combustion Science and Technology
http://dx.doi.org/10.1080/00102202.2019.1588261

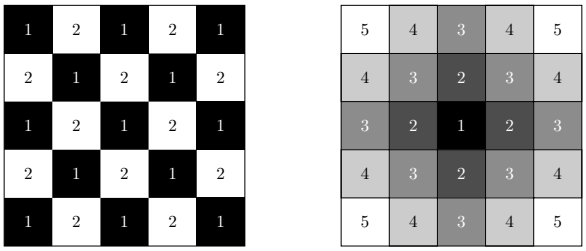

Figure 5: The checkerboard algorithm is illustrated on the left. The subsets of minimization are alternated between layers and from time step to time step. To the right the iteration process for the breadth-first search based on the center cell as the root is illustrated.

search (BFS) algorithm has additionally been implemented and employed. The basic difference between the checkerboard and the BFS algorithm is that the order in which the least-squares method is applied to the 3DCVs is different. A series of simulations has been conducted to demonstrate the effects of the different iteration procedures, with the results shown in Section 3. In more detail the alternative algorithms are given by:

- **The checkerboard algorithm:** By the minimization algorithm, final values of the displacements across all interfaces of the 3DCVs are determined by a checkerboard routine for each layer of 3DCVs. Since neighbouring 3DCVs share a common face, the minimization of the residuals Ξ_l is only feasible, but also sufficient, when the 3DCVs belong to one of the two checkerboard subsets of the set of all 3DCVs in each layer, as illustrated in the left-hand side of Figure 5. To ensure a consistent procedure, the selected checkerboard subset is alternated for each successive layer of 3DCVs, and also for successive time-advancement cycles.

- **The breadth-first search (BFS) algorithm:** Originally developed by Zuse (1972) and employed here to ensure a smooth spatial distribution of the deviations. The Manhattan Metric[1] is applied as the measure of distance, and the main cell of interest for each layer as the root of the search. The right-hand side of Figure 5 illustrates the iteration procedure, exemplified by the center cell as the root.

As shown in Section 3, the simulations are not only sensitive to the choice of minimization procedure, but also to the choice of the root in the BFS algorithm.

2.5. RANS simulation

The initial steady-state RANS simulations of the vitiated co-flow burner to provide mean-flow information to LEM3D are here performed by employing the ANSYS Fluent package, which solves the Reynolds-Averaged Navier-Stokes equations for the mean conservation of mass, momentum and energy, together with the k-ε

[1]Let $x = (x_1, \ldots, x_n)$ and $y = (y_1, \ldots, y_n) \in \mathbb{R}^n$. Then the Manhattan metric is defined as $d(x, y) = \sum_{i=1}^{n} |x_i - y_i|$.

This is the accepted version of an article published in Combustion Science and Technology
http://dx.doi.org/10.1080/00102202.2019.1588261

turbulence model equations. The RANS simulations are performed on a cuboidal 75×75×60 grid, employing a modified k-ε model.

The jet inlet is approximated by a single cell, where the area of the jet is preserved, i.e., $(\Delta x)^2 = \pi(d/2)^2$, where d is the jet diameter and Δx is the mesh size. The effect of using a square nozzle in this study is assumed to be negligible, justified by an experimental study for a similar burner configuration which indicated that changing from a blunt-edge nozzle to a tapered nozzle bears no discernible impact on the lift-off height L (North et al., 2014). The lack of sensitivity of L on the nozzle geometry is explained by that the lifted flame is sufficiently far away from the nozzle, that is $L/d \geq 10$, with negligible impact on L from local recirculation around the nozzle exit. The coarse RANS grid is a somewhat crude approximation, but is chosen here to demonstrate the potential of LEM3D as a post-processing tool to give additional details of the reactive flow.

The numerical scheme used for the RANS simulations is given in Table 1. Both a cold-flow jet without reactions and the lifted jet flame configuration are examined here, and the same numerical conditions are used for the two cases. Thus, the steady-state flow field for the lifted flame is obtained by starting from the converged cold-flow field and running to convergence again after the reactions have been switched on. A modified k-ε model is employed, with the constant $C_{2\varepsilon}$ set as in Myhrvold et al. (2006) to correct for the overestimated spreading rate for round jets by the standard k-ε model (Christo and Dally, 2005). The chemistry is solved using the Eddy Dissipation Concept (EDC) model, which includes detailed chemical kinetics in turbulent flows. Here, the H_2/O_2 mechanism of Li et al. (2004) is employed. In the EDC model, the chemical reactions are assumed to take place in small turbulent structures called fine-structure regions (Magnussen, 1981; Ertesvåg and Magnussen, 2000). The boundary conditions used in the computations are detailed in Table 2, and these are the same as used in the simulations by Cabra et al. (2002) and by Myhrvold et al. (2006). A series of initial RANS simulations showed that the lift-off height was extremely sensitive to the turbulent Prandtl number σ_h and the turbulent Schmidt number σ_{Y_i}, and the values of these numbers were tuned to obtain a lift-off in agreement with the Cabra experiment. Thus, with the conditions shown in Table 1 and Table 2, the RANS simulation converged to a flame with a lift-off height $L = 10.2\,d$ while Cabra et al. (2002) measured a lift-off of $L = 10\,d$ in the burner configuration. The lift-off is defined as the axial location where the OH mass fraction first reaches 600 ppm as used in Cabra et al. (2002), Cabra (2003), and Myhrvold et al. (2006).

During the RANS simulations, certain issues were encountered with respect to flame stabilization. This seems to be due to hysteresis effects. Hysteresis on $T_{\text{co-flow}}$, V_{jet}, and the dilution level $y_{\text{N}_2,\,\text{jet}}$ affects the stability regimes layout, though for the vitiated co-flow burner stability is most sensitive to $y_{\text{N}_2,\,\text{jet}}$. These hysteresis effects influencing the transition to the lifted condition are well known and documented (Lyons, 2007). However, it is reported for a lifted flame with similar conditions that the hysteresis effect will not affect the stability boundaries in the unsteady regime (North, 2013).

This is the accepted version of an article published in Combustion Science and Technology
http://dx.doi.org/10.1080/00102202.2019.1588261

2.6. The hybrid RANS-LEM3D model

The hybrid model is based on an initial RANS simulation in the Fluent Solver which generates the necessary model input to LEM3D. The RANS model input to LEM3D is mean-flow information such as the mean mass flux $\overline{\rho}\overline{\boldsymbol{u}}$ and the turbulent diffusivity D_T of the flow field. The mean mass flux governs the advective transport of scalars in LEM3D, while the turbulent diffusivity governs the turbulent advection (stirring) by determining the rate at which turbulent eddy events occur. Both the mass flux and the turbulent diffusivity typically vary in the spatial directions, but are resolved only at the coarser length scale corresponding to the 3DCVs. The values of D_T are fed to the centers of the control volumes, while face-normal components of $\overline{\rho}\overline{\boldsymbol{u}}$ are provided to the 3DCV faces. The turbulent diffusivity is given by the turbulent viscosity ν_T by

$$D_T = \frac{\nu_T}{\sigma_T} = \frac{C_\mu}{\sigma_T}\frac{k^2}{\varepsilon}, \tag{11}$$

where σ_T is the turbulent Schmidt number (or the Prandtl number when referring to the temperature field), and $C_\mu = 0.09$ (Launder and Spalding, 1974).

Additional model inputs to LEM3D include local values for the integral length scale L_{int} and the Kolmogorov scale η, as well as a value for the scaling exponent p that governs the eddy-size dependence in the Kolmogorov inertial cascade range. The integral and Kolmogorov scale are calculated from the k-ε model, respectively given by

$$L_{\text{int}} = C_\mu \frac{k^{3/2}}{\varepsilon}, \tag{12}$$

and

$$\eta = L_{\text{int}} \left(\frac{\nu_M}{\nu_T}\right)^{\frac{3}{4}}. \tag{13}$$

The scaling exponent p used in the linear eddy model framework is based on the scaling relation of the turbulent viscosity $\nu_T(l) \propto l^p$, as induced by turbulent eddies of size l or smaller. The scaling exponent is set to $p = 4/3$ on the basis of the inertial range scaling law (Richardson, 1926; Tennekes and Lumley, 1972).

Table 3: LEM3D input properties

Physical parameters		Model parameters	
Δx	4.05×10^{-3} m	CFL	0.1
Δt	1.25×10^{-6} s	fac	4
Δx_w	5.19×10^{-5} m	LEM_{res}	78
p	1 bar	p	4/3

We here demonstrate the RANS-LEM3D coupling using a coarse steady-state RANS simulation in Fluent for which there is a one-to-one correspondence between the RANS grid cells and the 3DCVs. The LEM3D simulation domain is a cuboidal 31×31×50 grid and thus a sub-domain of the Fluent domain. In this case, no interpolation is needed and the values of the turbulent diffusivity and the face-normal velocity components are used as direct input to LEM3D. The input profiles are obtained by user-defined functions (UDFs) in Fluent

This is the accepted version of an article published in Combustion Science and Technology
http://dx.doi.org/10.1080/00102202.2019.1588261

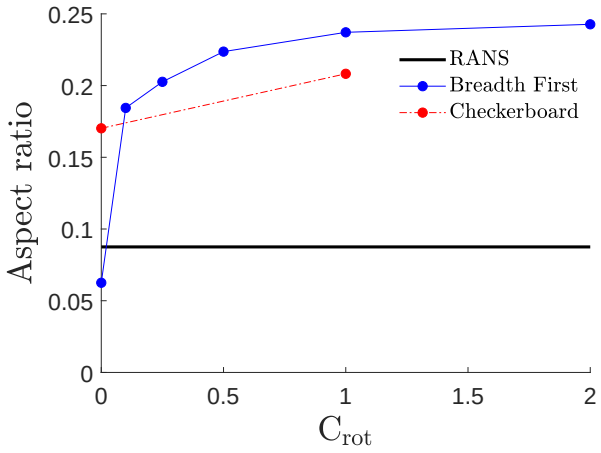

Figure 6: The aspect ratio for the different iteration schemes and values of C_{rot}. The aspect ratio is calculated from the (max. width)/height of the iso-surface $\widetilde{Y}_{\mathrm{H_2}} = 0.01$.

which format the data in line with the proper input format for LEM3D. The LEM3D simulation is performed with the conditions presented in Table 3, where the parameter fac is an under-resolving parameter available for computational saving. Hence, we resolve down to the minimum of $(\mathrm{fac} \cdot \eta)$ in the entire domain, which implies that the number of wafers within the 3DCVs in each coordinate direction is $\mathrm{LEM}_{\mathrm{res}} = \Delta x / \min(\mathrm{fac} \cdot \eta)$. The time advancement is calculated from the CFL number through $\Delta t = \mathrm{CFL}\, \Delta x / \max(|\boldsymbol{u}|)$. Note that the above settings are done for simplicity and that any RANS grid could be interpolated into a suitable mesh for LEM3D.

3. Results and Discussion

The coupling of the LEM domains were discussed in sub-section 2.4. In this section we examine three different iteration procedures and the effects of varying C_{rot} within these;

- The checkerboard without least squares (CB)
- The breadth first with least squares and the root taken as the jet-nozzle (BFS)
- The breadth first with least squares and the root given where the reactions first take place, i.e., the highest concentration of the radical H_2O_2, (BNC).

3.1. Cold flow

We first examine how well LEM3D performs for a flow field without reactions, given the numerical scheme of Table 1 and the boundary conditions of Table 2. In Figure 6, the aspect ratio based on the (max. width)/height of the iso-surface $\widetilde{Y}_{\mathrm{H_2}} = 0.01$ is shown. We observe that a smaller C_{rot}, i.e., a weaker coupling between the domains, results in smaller aspect ratios. Further, for all values of C_{rot}, other than zero, breadth first has a higher aspect ratio than the checkerboard routine. These results coincide well with

This is the accepted version of an article published in Combustion Science and Technology
http://dx.doi.org/10.1080/00102202.2019.1588261

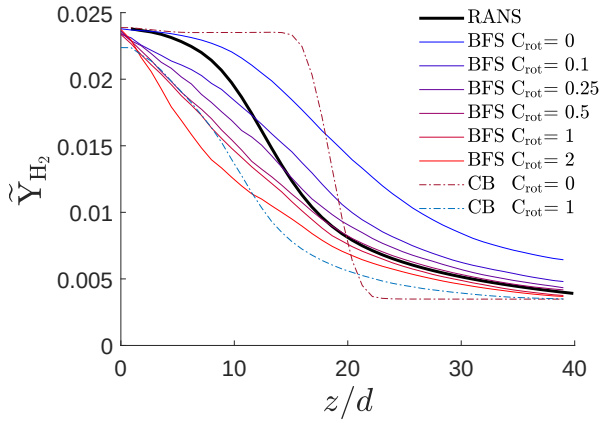

Figure 7: Axial profiles of H_2 for the different iteration routines and values of C_{rot}, time-averaged iterations over 20000 iterations smoothed (i.e. averaged over each 3DCV cell).

the contours of both species and temperature (not shown here), and indicate that a higher value of C_{rot} induces more diffusion of hydrogen out on the domains surrounding the centerline.

Figure 7 shows the centerline profiles of the H_2 mass fraction resulting from the iteration procedures for different C_{rot}, sampled 20 times at a sampling frequency of every 1000 iterations or approximately two flow-through times. The resulting time-averaged solution is then averaged to 3DCV resolution for comparison with RANS. We observe in the downstream region, i.e. for $z/d > 20$, that all the profiles, except for $C_{\text{rot}} = 0$, coincide well with RANS. However, in the upstream region $z/d < 6$, only the $C_{\text{rot}} = 0$ profile has a similar decay as the RANS solution. Furthermore, we note that especially the checkerboard $C_{\text{rot}} = 0$ procedure has an inaccurate solution with a rapid drop in the range $z/d \in [10, 20]$. It should also be noted that there is a clear trend, as in Figure 7, that for smaller C_{rot} we have less diffusion away from the centerline. Overall, the breadth first with $C_{\text{rot}} = 0.25$ is observed to yield the most accurate trends in addition to being consistent with RANS. The breadth-first approach generally coincides more than the previously implemented checkerboard scheme for the axial profiles, indicating that the new solution procedure is an improvement to the model.

To illustrate the increased information and enhanced resolution given by LEM3D, an instantaneous axial profile of $\widetilde{Y}_{H_2}$ is shown in Figure 8. The profile is sampled after convergence of the breadth-first routine with $C_{\text{rot}} = 0.25$. We observe that the downstream profile coincides well with the RANS solution, while there is much more fluctuation in the H_2 concentration in the upstream domain, corresponding to effects of the turbulent stirring.

In Figure 9, time-averaged radial profiles of $\widetilde{Y}_{H_2}$ with 3DCV resolution at three axial positions of the jet are shown for the various iteration schemes. At $z/d = 7$, we observe that the profiles for lower values of C_{rot} become sharper and more similar to the RANS profile. However, all the profiles, except for the checkerboard $C_{\text{rot}} = 0$, predict more spreading of the hydrogen than RANS. At $z/d = 15$, we observe that this particular procedure for $C_{\text{rot}} = 0$ gives less spread in the downstream cells since the area below the graph clearly is

This is the accepted version of an article published in Combustion Science and Technology
http://dx.doi.org/10.1080/00102202.2019.1588261

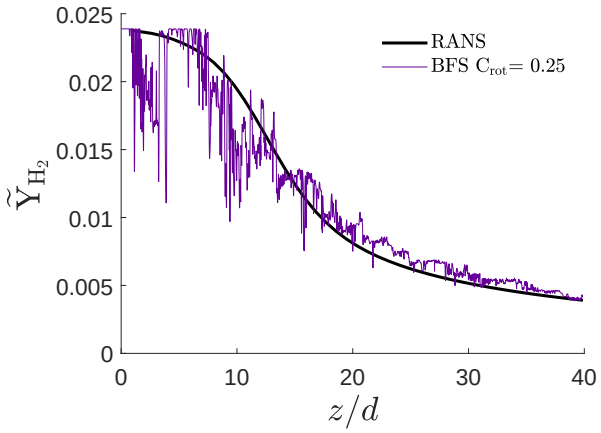

Figure 8: Instantaneous axial profile of H_2 of the breadth-first procedure with $C_{\mathrm{rot}} = 0.25$.

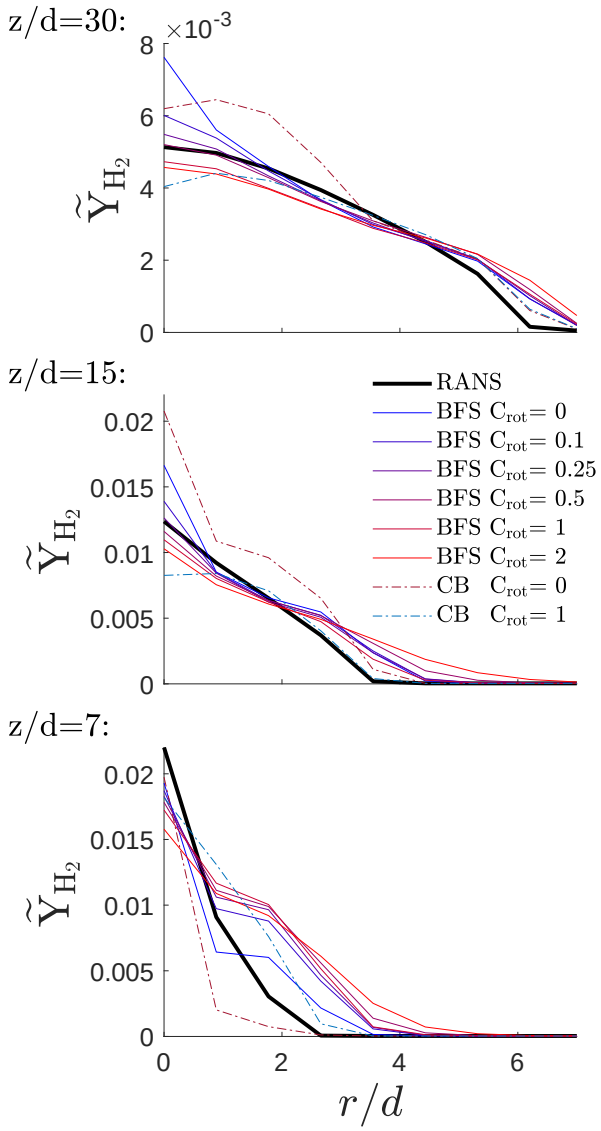

Figure 9: Radial profiles of H_2 at the three axial positions $z/d = 7$, 15 and 30.

This is the accepted version of an article published in Combustion Science and Technology
http://dx.doi.org/10.1080/00102202.2019.1588261

larger than any of the others. In general, the profiles get sharper with smaller C_{rot}. At $z/d = 30$, we see a clear indication that for both checkerboard schemes the advective coupling described in sub-section 2.4 is not strong enough to couple the 1D LEM domains satisfactorily. This may also be observed by considering the deviating mass flux Ξ_{flux} at the centerline compared to the surrounding domains. Thorough investigations have shown that at the centerline, Ξ_{flux} will be large in magnitude but negative, while in the neighboring domains Ξ_{flux} has a large positive magnitude. Hence, there is a deficit of advection down the centerline compared to the surrounding domains and we obtain the 'dip' as illustrated by the dashed-dotted lines for $z/d = 30$. This was indeed the reason for introducing the breadth-first scheme; that is to obtain an evenly distribution of Ξ_{flux}. Another inaccurate profile is from the breadth-first procedure with $C_{\text{rot}} = 0$. This routine gives a too sharp gradient compared to both RANS and to the other profiles. At $z/d = 30$, the breadth-first routine with $C_{\text{rot}} = 0.5$ coincides well with RANS for $r \in [-5, 5]$.

The observed decrease in H_2 with increasing C_{rot} has been thoroughly investigated. It has shown to be an artifact in the construction of the coupled 1D domains. With higher values of C_{rot}, we introduce more frequent sharp gradients in between the control volumes, simultaneously as we require rotation to couple the domain. Hence, an optimum needs to be estimated for each case. For non-reacting simulations, $C_{\text{rot}} = 0.25$ is generally preferable for the use of the breadth-first scheme while the checkerboard algorithm generally performs best with $C_{\text{rot}} = 1$. Overall, for the non-reacting simulation the breadth first $C_{\text{rot}} = 0.25$ procedure is found to give the most accurate time-averaged match with the RANS profiles and would hence be the most beneficial for post-processing of RANS.

3.2. Lifted flame

We here consider the same set-up as in sub-section 3.1, but with chemical reactions as described in sub-section 2.3. For the reactive study we include the breadth-first iteration scheme with the root determined by where the reactions take place, i.e., at the highest concentration of the radical H_2O_2 (BNC).

In Figure 10, the lift-off height and non-reacting flame volume are shown versus C_{rot} for the different iteration schemes used in the reacting case. The non-reacting flame volume is calculated using the Riemann-integral of the volume enclosed by the upstream concave surface defined along the iso-lines of $\widetilde{Y}_{\text{OH}} = 600$ ppm and its normals down to the inlet plane. Notice that this surface will contain the lift-off point. The non-reacting flame volume (NRFV) is defined by

$$\text{NRFV} = \int_{\theta=0}^{2\pi} \int_{r=-R_L}^{R_L} H(r,\theta)\ dr d\theta, \tag{14}$$

where R_L denotes the radial position of the lift-off point and $H(r,\theta)$ is a function giving the flame-front normalized by the jet diameter. Here, $H(r,\theta)$ is defined as the time-averaged iso-line of $\widetilde{Y}_{\text{OH}} = 600$ ppm at points (r,θ).

We observe that both parameters, i.e., the lift-off height L and the NRFV indicate that the simulations yield different profiles than the RANS solution. The lift-off L increases somewhat with decreasing C_{rot}, while

This is the accepted version of an article published in Combustion Science and Technology
http://dx.doi.org/10.1080/00102202.2019.1588261

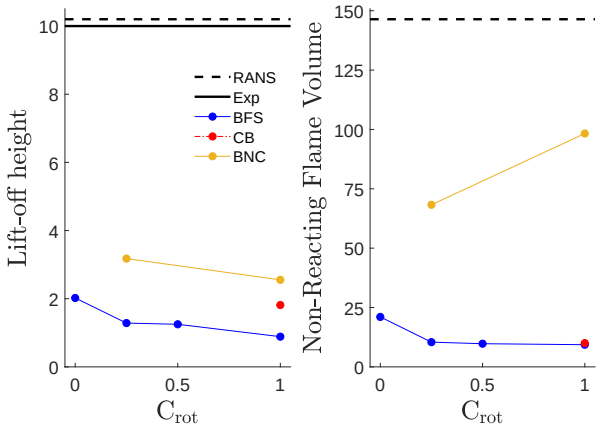

Figure 10: Lift-off height (L/d) and the non-reacting flame volume vs. C_{rot} and the different iteration regimes for the reacting case.

the trend is not equally clear for NRFV. However, using the BNC as the iteration procedure results in a better agreement with the experiments and RANS. For all cases, we also note that the NRFV gives a more accurate prediction in comparison to the lift-off alone when it comes to describing the flame shape. The NFRV accounting for the inaccurate jet-penetration into the flame, typically seen for values of C_{rot} close to and equal to zero, while the lift-off height just indicate the first occurrence of $\widetilde{Y}_{\mathrm{OH}} = 600$ ppm. This inaccurate jet-penetration can be seen e.g. in the contours of BFS $C_{\mathrm{rot}} = 0.25$ in Figure 11.

3.2.1. Contour plots

The OH contours of Figure 11 show the various flame shapes based on the 3DCV-averaged solutions for the different iteration schemes. The leftmost sub-figure show the profile of the RANS simulation, supporting the contours of Myhrvold et al. (2006). In the second sub-figure from the left, the checkerboard scheme with $C_{\mathrm{rot}} = 1$ yields an inaccurate dip on the centerline of the contour. This dip, which is also present in the mixture fraction contours (not shown here), indicates that the jet fuel almost vanishes from centerline at this axial location. This is a result of the lack of sufficient entrainment to the centerline provided by the checkerboard scheme, letting the jet disperse out of the centerline to the neighboring domains. As a consequence, there are enhanced reactions in the domains surrounding the centerline at the expense of possible centerline reactions, and hence the dilatations are too small in the centerline domain and too large in the surrounding domains. The mass flux deviation Ξ_{flux} of Eq. (10) is the largest where the reactions take place, and hence the 1D domains containing enhanced reactions will impose large deviations in these domains. Thus, Ξ_{flux} will be large in the domains surrounding the centerline, while Ξ_{flux} along the centerline domain is enforced to have large, negative values. The checkerboard scheme therefore gives an advection deficit along the centerline, explaining the inaccurate dip mentioned above. The three rightmost sub-figures of 11 display the flame structures for various breadth-first schemes, all with a more accurate appearance than the checkerboard scheme.

As discussed in sub-section 3.2, the various LEM3D simulations all give a low lift-off height compared to

This is the accepted version of an article published in Combustion Science and Technology
http://dx.doi.org/10.1080/00102202.2019.1588261

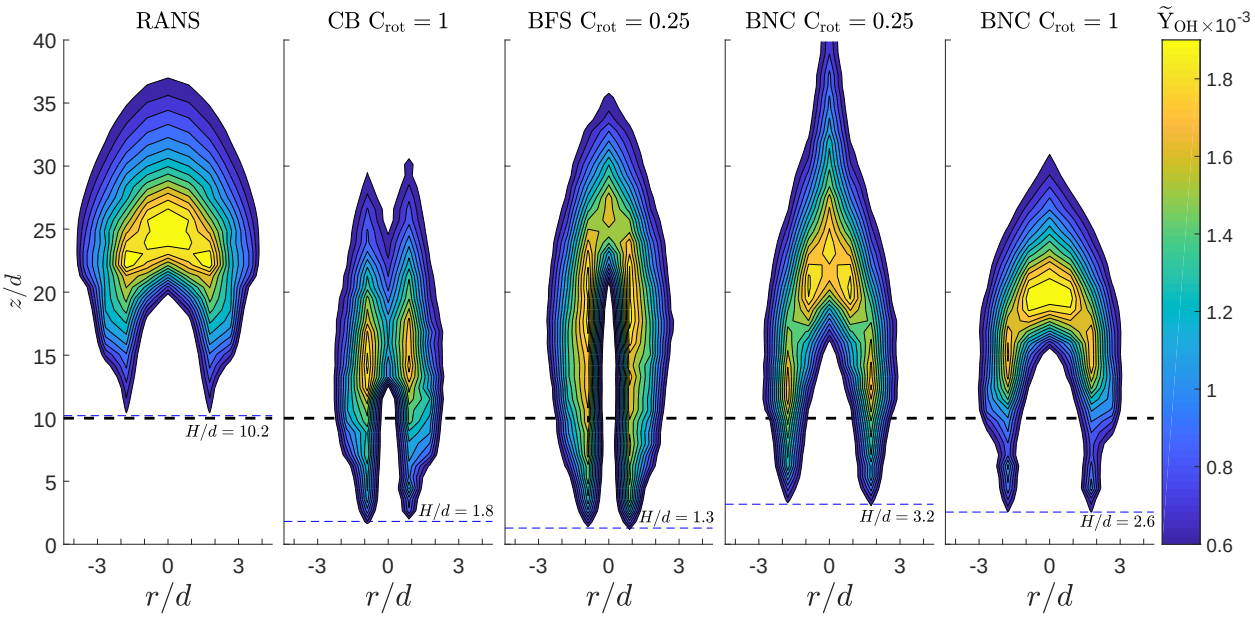

Figure 11: OH contour plots of the RANS and the four iteration schemes investigated in this section. The black line indicates the experimental lift-off $H/d = 10$, and the blue line indicates the lift-off for the given simulation.

both RANS and the experiments (Cabra et al., 2002). However, as indicated by the experimental contours shown in Cabra et al. (2002) and Cabra (2003), the radial stabilization of the lift-off point occurs at about $r/d = 1.2$ and this is reflected both by the CB and BFS iteration schemes. In this regard, both the BNC profiles and the RANS stabilize at a wider radial distance of $r/d \approx 1.8$. The experimental measurements also indicate that below $z/d = 25$ the width of the flame is no wider than $r/d \approx 2$. The RANS here gives a width as large as $r/d = 3.8$, while all of the LEM3D simulations provide a width in the range $r/d \in [2.1, 2.8]$. It should be noted that the overspreading is a known problem and that all models in Cabra et al. (2002) and Myhrvold et al. (2006) over-predict the width of the flame stabilization region compared to experiments. Concerning the overall flame structure, here illustrated by the shape of the 600 ppm iso-contours, the breadth-first scheme with root not in the center produces OH contours that seem to have the most accurate and comparable shape to experiments.

3.2.2. Axial profiles

Centerline profiles of the mixture fraction, the temperature and the density-averaged mass fractions of O_2, H_2O, H_2, and OH for the lifted flame obtained with various iteration procedures are compared to experimental data and shown in Figure 12. The axial profiles are based on 20 time-averaged samples and averaged to 3DCV resolution for comparison with RANS. It should be noted that since the LEM3D schemes predict a smaller lift-off than RANS, as indicated by Figures 10 and 11, the profiles are expected to be shifted.

The mixture fraction ξ is computed using Bilger's formula based on the elemental mass fractions of the

This is the accepted version of an article published in Combustion Science and Technology
http://dx.doi.org/10.1080/00102202.2019.1588261

fuel and oxidizer (Bilger, 1989), i.e.,

$$\xi = \frac{0.5\, Z_{\mathrm{H}}/W_{\mathrm{H}} + (Z_{\mathrm{O},0} - Z_{\mathrm{O}})/W_{\mathrm{O}}}{0.5\, Z_{\mathrm{H},F}/W_{\mathrm{H}} + Z_{\mathrm{O},0}/W_{\mathrm{O}}}, \tag{15}$$

where the subscripts F and O denote the fuel and the oxidizer streams, W is the molecular weights, and Z_{H} and Z_{O} are elemental mass fractions of hydrogen and oxygen, respectively.

As seen from the profiles, the BNC and the BFS curves generally follow similar trends with some differences in the axial location of the peaks of the H_2O, OH, and temperature profiles. For the mixture fraction, there is good agreement between these curves, the RANS, and the experimental results. The CB curves basically fail in predicting the experimental trends correctly. The value of the OH peak is generally over-predicted by a factor of two for all the simulations (including the RANS).

As discussed by Myhrvold et al. (2006), the results for the axial O_2 profiles are related to the predicted lift-off height. Since the RANS simulation with the modified k-ε model gave a lift-off of $L = 10.2\, d$, it allows for more diffusion of O_2 towards the centerline since the oxygen is consumed by the flame at a later axial location than for the LEM3D simulations. The O_2 peak illustrates the downstream penetration and subsequent consumption of the O_2. The peak is generally higher for models that predict higher lift-off since there is a slower consumption of O_2 and hence more oxygen is diffused to the centerline. Except for the BFS iteration scheme, the CB and BNC schemes of LEM3D yield an earlier reaction at the centerline as observed from the contours of Figure 11. The earlier reaction is also observed by the earlier consumption of H_2, an earlier OH peak, and consequently an earlier production of H_2O as shown in Figure 12.

The profiles of Figure 13 are instantaneous LEM resolved profiles compared to RANS and the experimental values. The trend with the difference in predicted lift-off is more evident here, as it is clear that the overall shape agrees for all profiles but are shifted a distance $7.4\, d$ upstream compared to the experimental lift-off. As discussed in the previous paragraph, the under-prediction of the lift-off results in no primary peak of the O_2-profile. Further, we observe that most of the larger eddies occur, as expected from the flow field (not plotted here), in the range $z/d \in [5, 20]$.

3.2.3. Scatter plots

In this section, scatter plots comparing experimental results to the best performing scheme, i.e., the breadth first with least squares and the root given were the reactions first take place, are discussed. Figure 14 shows scatter data of the temperature versus the mixture fraction at five different axial positions, $z/d \in \{8, 9, 10, 11, 26\}$, together with theoretical values for mixing without reaction and adiabatic equilibrium for comparison. The right-hand side of Figure 14 shows experimental results. Approximately 4000 point measurements were grouped together from different radial positions to form a probability density map. The left-hand side gives the LEM3D scatter data based on small-scale wafer resolution (black dots), 3DCV averaged results (green dots), and the underlying RANS results for the simulation (blue dots). The LEM resolved results are sampled for each point at the plane normal to the jet for each of the axial positions in a single time step after convergence.

This is the accepted version of an article published in Combustion Science and Technology
http://dx.doi.org/10.1080/00102202.2019.1588261

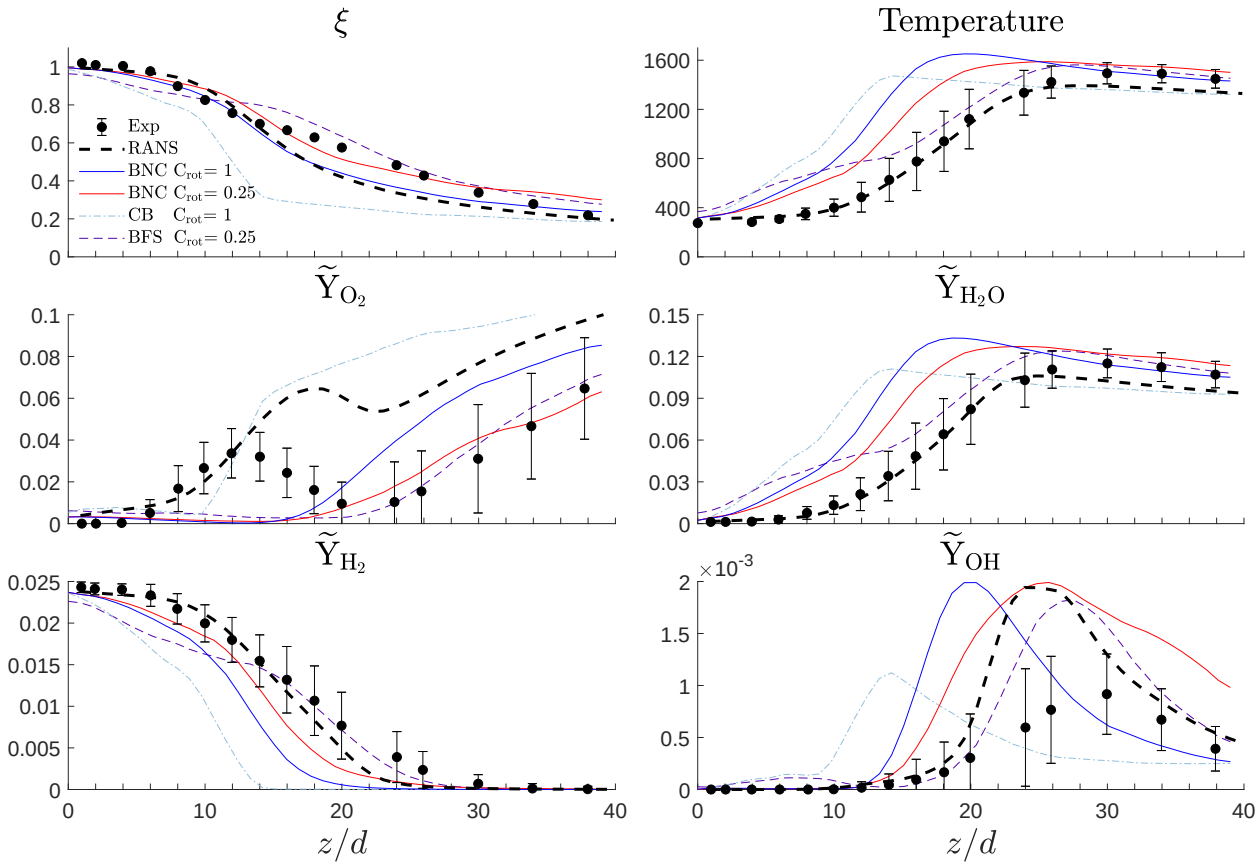

Figure 12: Axial profiles of various scalars shown for the different iteration routines and compared with RANS and the experimental results to illustrate. The profiles are based on a time-averaged solution over 20 samples and smoothed to 3DCV resolution. The mixture fraction profile fits very well with the measurements, while there are various differences for the other curves.

This is the accepted version of an article published in Combustion Science and Technology
http://dx.doi.org/10.1080/00102202.2019.1588261

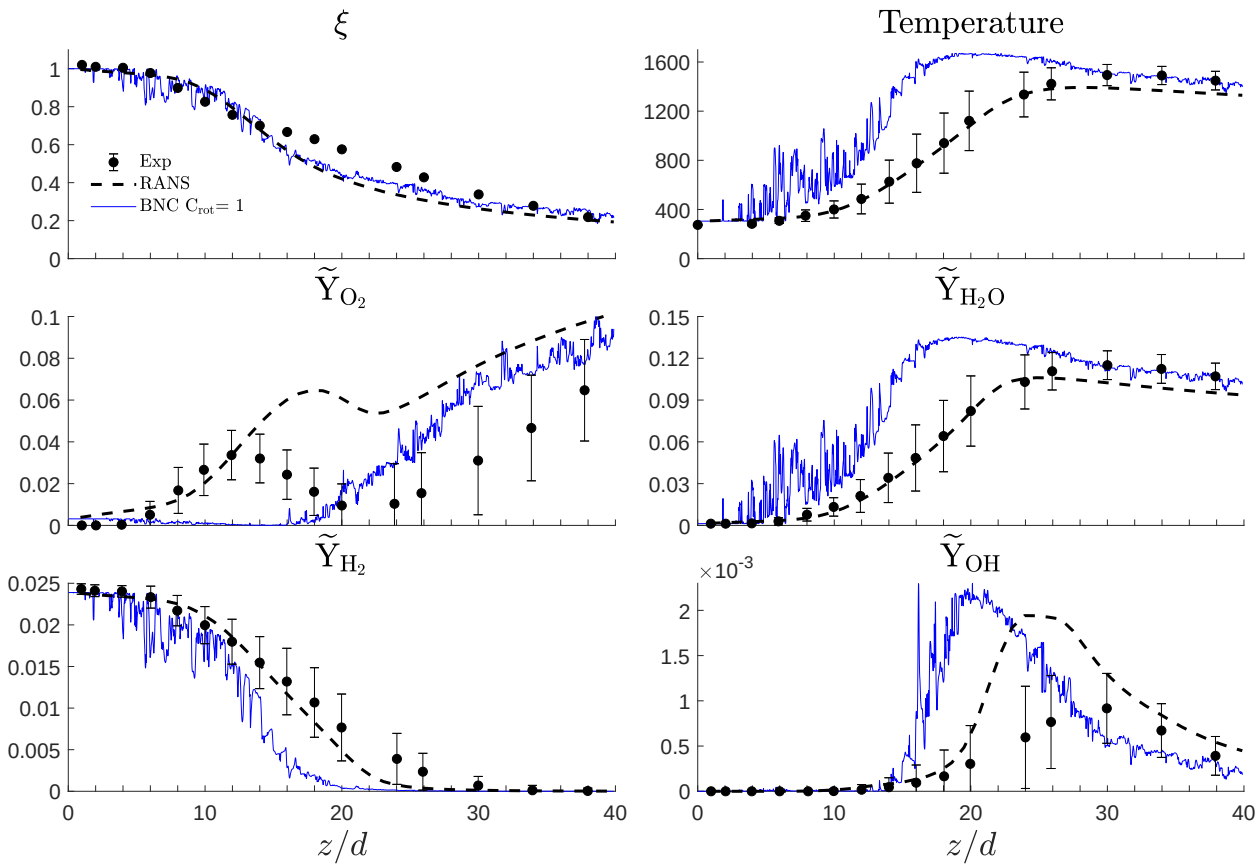

Figure 13: Axial LEM-resolved instanteous profiles of various scalars after convergence.

This is the accepted version of an article published in Combustion Science and Technology
http://dx.doi.org/10.1080/00102202.2019.1588261

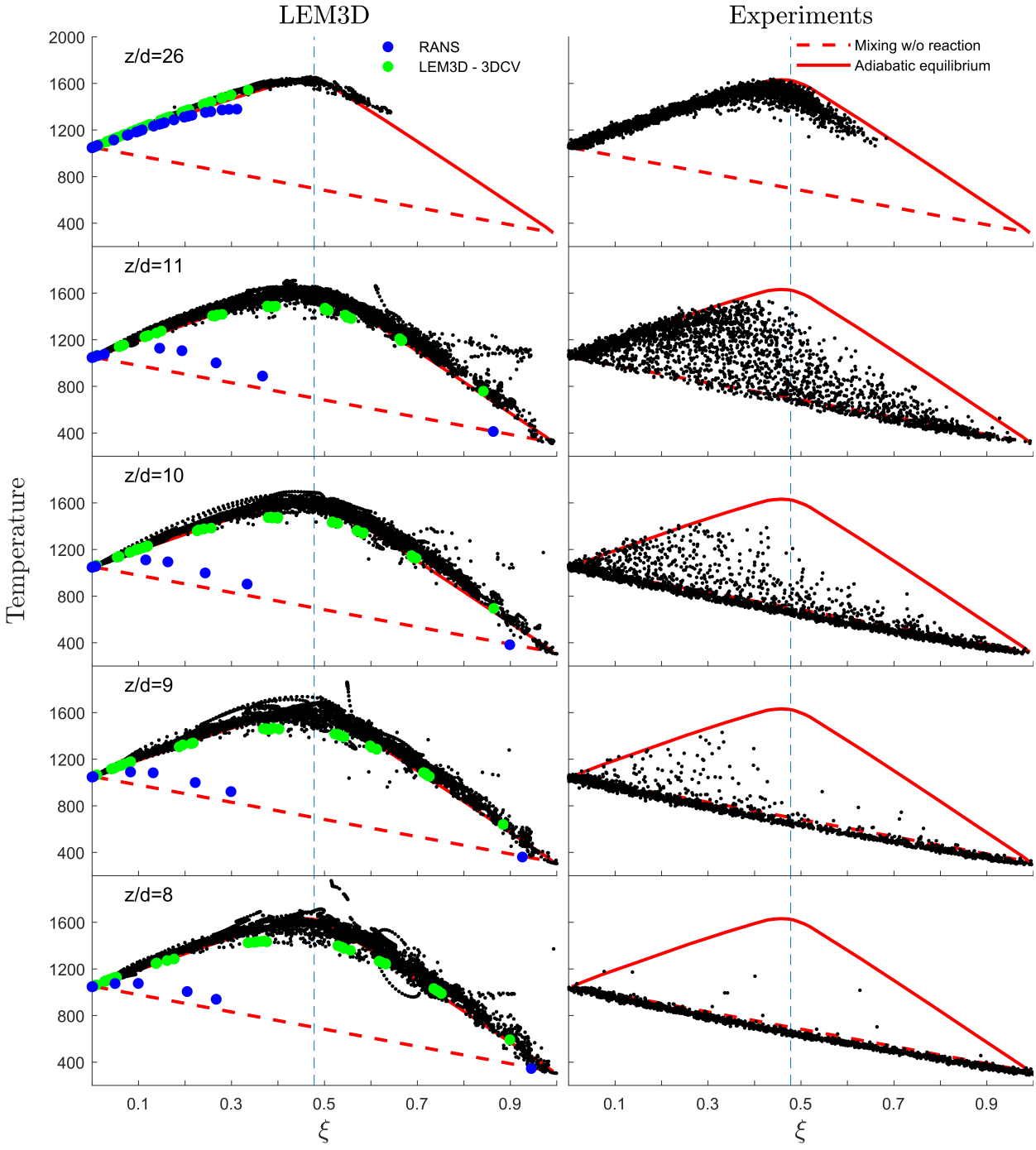

Figure 14: Scatter data of the temperature versus the mixture fraction at five axial positions of both LEM3D and RANS (left), and the experiments conducted by Cabra et al. (2002) (right). The red curves indicate theoretical values for mixing without reaction and adiabatic equilibrium. For the left side of the figure, the blue, the red and the black dots show the underlying RANS solution to LEM3D (initial values for the simulation), the 3DCV averaged values for LEM3D, and the LEM-resolved values, respectively.

This is the accepted version of an article published in Combustion Science and Technology
http://dx.doi.org/10.1080/00102202.2019.1588261

None of the flames are attached to the nozzle, but at $z/d \approx 8$ where hot O_2 from the co-flow are getting entrained in the experiments, evolving into a partially premixed flow with fluid temperatures corresponding to the mixing line between the jet and the co-flow boundary conditions, the mixing in LEM3D seems already to have approached a fast chemistry limit. Since the LEM3D iteration schemes yield small lift-offs, the flame structure is different compared to the experiments. While in the experiments there is a clear progression from a predominantly mixing condition to a vigorous flame burning that corresponds to the transition from mixing only to mixing combined with ignition and flame stabilization, the LEM3D scheme tends to lay close to the adiabatic equilibrium limit and thus indicates a too high rate of reactions.

For both scatters there is progressive dilution of the richest samples beyond the potential core of the jet, such that the fuel-rich boundary condition for combustion gradually decreases from $\xi = 1$ to values $\xi \in [0.6, 0.7]$. Again, as for the axial profiles, we observe that the data tend to be in better agreement in the far-field region than in the near field.

4. Conclusions

The focus of the present work has been to demonstrate the LEM3D with the novel breadth-first iteration scheme and to test the model capabilities vs. RANS and experimental measurements. The LEM3D model has here been applied to a turbulent lifted hydrogen jet flame in a vitiated co-flow. LEM3D contributes information not available from RANS alone, e.g., scatter plots and instantaneous profiles. This kind of information may be of practical importance for predicting flame behavior in industrial combustion applications.

Even though LEM3D shows good agreement with experiments in the far field, currently the algorithms do not yield a lift-off height in accordance with the experiments. Thorough investigations of this issue have shown that the rotations are causing an increased spread of H_2, as most easily observed in the non-reactive case. Combined with low fluxes in the LEM domains surrounding the central jet nozzle, and the treatment in LEM3D of three dimensions as 3×1D, the conditions and residence times are sufficient for reactions, stabilizing the flame at a low lift-off. However, near-field discrepancy is a previously known model artifact of LEM resulting from the instantaneous nature of the eddy events (Kerstein, 1992), and among other things the undeveloped energy spectrum.

LEM3D is further shown to be sensitive to numerical implementation details such as the coupling scheme and the rotation factor C_{rot}. Possible improvements in this regard are noted. The sensitivity cannot be thoroughly evaluated here because the chosen application constrains important aspects of numerical implementation. Other such sensitivities have been examined for simple flows (Weydahl, 2010) and mixing without chemical reactions (Sannan et al., 2013).

To a large degree, the limitations of LEM3D in this context are a result of the reliance on RANS-type steady-state inputs rather than concurrent unsteady time advancement of LEM3D coupled to LES. Though this would undoubtedly improve model performance, as indicated by previous LEM-LES applications, the

This is the accepted version of an article published in Combustion Science and Technology
http://dx.doi.org/10.1080/00102202.2019.1588261

present goal is to assess the degree of improvement of RANS performance for mixing and combustion applications that can be achieved by introducing LEM closure. Any such improvement would be beneficial due to the relatively low cost and wide usage of RANS.

While previous studies and the experimental data did not have clear evidence of autoignition events below the lift-off height, it was seen in the current work that autoignition, or turbulent mixing of products and reactants in the stabilization region followed by rapid ignition, seemed to cause stability in LEM3D.

Acknowledgments

This work at the Norwegian University of Science and Technology and Sintef Energy Norway was supported by the Research Council of Norway through the project HYCAP (233722). The authors would also like to thank Alan R. Kerstein for numerous, invaluable discussions and support.

Compliance with Ethical Standards

Conflict of interests The authors declare that they have no conflict of interest.

References

Bilger, R., 1982. Molecular Transport Effects in Turbulent Diffusion Flames at Moderate Reynolds number. AIAA Journal 20 (7), 962–970.

Bilger, R., 1989. The Structure of Turbulent Nonpremixed Flames. Proc. Comb. Inst. 22, 475–488.

Bird, R. B., Stewart, W. E., Lightfoot, E. N., 1960. Transport Phenomena. John Wiley & Sons.

Bisetti, F., Chen, J.-Y., Chen, J. H., Hawkes, E. R., 2009. Differential diffusion effects during the ignition of a thermally stratified premixed hydrogen–air mixture subject to turbulence. Proceedings of the Combustion Institute 32 (1), 1465–1472.

Brown, P. N., Byrne, G. D., Hindmarsh, A. C., 1989. VODE: A Variable-Coefficient ODE solver. SIAM journal on scientific and statistical computing 10 (5), 1038–1051.

Burke, M. P., Chaos, M., Ju, Y., Dryer, F. L., Klippenstein, S. J., 2012. Comprehensive H2/O2 kinetic model for high-pressure combustion. International Journal of Chemical Kinetics 44 (7), 444–474.

Cabra, R., 2003. Turbulent Jet Flames Into a Vitiated Coflow. Ph.D. thesis, University of California, Berkeley.

Cabra, R., Myhrvold, T., Chen, J., Dibble, R., Karpetis, A., Barlow, R., 2002. Simultaneous laser Raman-Rayleigh-Lif measurements and numerical modeling results of a lifted turbulent H2/N2 jet flame in a vitiated coflow. Proc. Comb. Inst. 29, 1881–1888.

Cao, R. R., Pope, S. B., Masri, A. R., 2005. Turbulent lifted flames in a vitiated coflow investigated using joint PDF calculations. Combustion and flame 142, 438–453.

Chakravarthy, V., Menon, S., 2000. Subgrid Modeling of Turbulent Premixed Flames in the Flamelet Regime. Flow, Turbulence and Combustion 65 (2), 133–161.

Christo, F. C., Dally, B. B., 2005. Modeling turbulent reacting jets issuing into a hot and diluted coflow. Combustion and Flame 142 (1-2), 117–129.

Dagaut, P., Lecomte, F., Mieritz, J., Glarborg, P., 2003. Experimental and Kinetic Modeling Study of the Effect of NO and SO2 on the Oxidation of CO-H2 Mixtures. International Journal of Chemical Kinetics 35 (11), 564–575.

Ertesvåg, I. S., Magnussen, B. F., 2000. The Eddy Dissipation Turbulence Energy Cascade Model. Combustion science and technology 159 (1), 213–235.

Goldin, G. M., Menon, S., Calhoon, Jr, W. H., 1995. A linear eddy mixing model for steady non-premixed turbulent combustion. In: 33rd Aerospace Sciences Meeting and Exhibit. p. 379.

Hawkes, E. R., Sankaran, R., Sutherland, J. C., Chen, J. H., 2005. Direct numerical simulation of turbulent combustion: fundamental insights towards predictive models. In: Journal of Physics: Conference Series. Vol. 16. IOP Publishing, p. 65.

Johannessen, B., North, A., Dibble, R., Løvås, T., 2015. Experimental studies of autoignition events in unsteady hydrogen–air flames. Combustion and Flame 162, 3210–3219.

Kerstein, A. R., 1988. A linear-eddy model of turbulent scalar transport and mixing. Combustion Science and Technology 60 (4-6), 391–421.

Kerstein, A. R., 1991. Linear-eddy modelling of turbulent transport. Part 6. Microstructure of diffusive scalar mixing fields. Journal of Fluid Mechanics 231, 361–394.

Kerstein, A. R., 1992. Linear-eddy modelling of turbulent transport. Part 7. Finite-rate chemistry and multi-stream mixing. Journal of Fluid Mechanics 240, 289–313.

Kerstein, A. R., 1999. One-dimensional turbulence: model formulation and application to homogeneous turbulence, shear flows, and buoyant stratified flows. Journal of Fluid Mechanics 392, 277–334.

Kerstein, A. R., 2002. One-dimensional turbulence: A new approach to high-fidelity subgrid closure of turbulent flow simulations. Computer Physics Communications 148 (1), 1–16.

Konnov, A. A., 2008. Remaining uncertainties in the kinetic mechanism of hydrogen combustion. Combustion and Flame 152 (4), 507–528.

This is the accepted version of an article published in Combustion Science and Technology
http://dx.doi.org/10.1080/00102202.2019.1588261

Launder, B. E., Spalding, D. B., 1974. The numerical computation of turbulent flows. Computer Methods in Applied Mechanics and Engineering 3 (2), 269–289.

Li, J., Zhao, Z., Kazakov, A., Chaos, M., Dryer, F. L., Scire, J. J., 2007. A comprehensive kinetic mechanism for CO, CH2O, and CH3OH combustion. International Journal of Chemical Kinetics 39 (3), 109–136.

Li, J., Zhao, Z., Kazakov, A., Dryer, F. L., 2004. An updated comprehensive kinetic model of hydrogen combustion. International Journal of Chemical Kinetics 36, 566–575.

Lyons, K. M., 2007. Toward an understanding of the stabilization mechanisms of lifted turbulent jet flames: Experiments. Progress in Energy and Combustion Science 33, 211–231.

Magnussen, B., 1981. On the structure turbulence and a generalized eddy dissipation concept for chemical reaction in turbulent flow. In: 19th Aerospace Sciences Meeting, St. Louis, MO, January 12-15, 1981.

Magnussen, B. F., 1989. Modeling of NO_x and Soot Formation by the Eddy Dissipation Concept. International Flame Research Foundation First Topic Oriented Technical Meeting.

Masri, A., Cao, R., Pope, S., Goldin, G., 2004. PDF calculations of turbulent lifted flames of H2/N2 fuel issuing into a vitiated co-flow. Combustion Theory and Modelling 8, 1–22.

Mastorakos, E., 2009. Ignition of turbulent non-premixed flames. Progress in Energy and Combustion Science 35 (1), 57–97.

McMurthy, P. A., Menon, S., Kerstein, A. R., 1992. A linear eddy sub-grid model for turbulent reacting flows: Application to hydrogen-AIR combustion. Symposium (International) on Combustion 24 (1), 271–278.

McMurtry, P. A., Gansauge, T. C., Kerstein, A. R., Krueger, S. K., 1993a. Linear eddy simulations of mixing in a homogeneous turbulent flow. Physics of Fluids A: Fluid Dynamics 5 (4), 1023–1034.

McMurtry, P. A., Menon, S., Kerstein, A., 1993b. Linear eddy modeling of turbulent combustion. Energy & Fuels 7 (6), 817–826.

Menon, S., Calhoon Jr, W. H., 1996. Subgrid mixing and molecular transport modeling in a reacting shear layer. Symposium (International) on Combustion 26 (1), 59–66.

Moo Lee, B., Dong Shin, H., 1988. Differential Diffusion Effects in H2/N2 Turbulent Nonpremixed Flames. Combustion Science and Technology 62 (4-6), 311–330.

Myhrvold, T., Ertesvåg, I., Gran, I., Cabra, R., Chen, J.-Y., 2006. A numerical investigation of a lifted H2/N2 turbulent jet flame in a vitiated coflow. Combustion Science and Technology 178, 1001–1030.

North, A., 2013. Experimental Investigations of Partially Premixed Hydrogen Combustion in Gas Turbine Environments. PhD thesis, University of California, Berkeley.

This is the accepted version of an article published in Combustion Science and Technology
http://dx.doi.org/10.1080/00102202.2019.1588261

North, A., Magar, M., Chen, J.-Y., Dibble, R., Gruber, A., 2014. Effect of Pressure, Environment Temperature, Jet Velocity and Nitrogen Dilution on the Liftoff Characteristics of a N2-in-H2 Jet Flame in a Vitiated Co-flow. Eurasian Chemico-Technological Journal 16 (2-3), 141–148.

Ó Conaire, M., Curran, H. J., Simmie, J. M., Pitz, W. J., Westbrook, C. K., Nov. 2004. A comprehensive modeling study of hydrogen oxidation. International Journal of Chemical Kinetics 36 (11), 603–622.

Olm, C., Zsély, I. G., Pálvölgyi, R., Varga, T., Nagy, T., Curran, H. J., Turányi, T., 2014. Comparison of the performance of several recent hydrogen combustion mechanisms. Combustion and Flame 161 (9), 2219–2234.

Punati, N., Sutherland, J. C., Kerstein, A. R., Hawkes, E. R., Chen, J. H., 2011. An evaluation of the one-dimensional turbulence model: Comparison with direct numerical simulations of CO/H2 jets with extinction and reignition. Proc. Comb. Inst. 33, 1515–1522.

Ranjan, R., Muralidharan, B., Nagaoka, Y., Menon, S., 2016. Subgrid-Scale Modeling of Reaction-Diffusion and Scalar Transport in Turbulent Premixed Flames. Combustion Science and Technology 188 (9), 1496–1537.

Richardson, L. F., 1926. Atmospheric diffusion shown on a distance-neighbour graph. Proceedings of the Royal Society of London. Series A, Containing Papers of a Mathematical and Physical Character 110 (756), 709–737.

Sankaran, V., Menon, S., 2005. Subgrid combustion modeling of 3-D premixed flames in the thin-reaction-zone regime. Proc. Comb. Inst. 30, 575–582.

Sannan, S., Kerstein, A. R., 2014. Numerical simulation of differential molecular diffusion effects in a hydrogen-rich turbulent jet using LEM3D. Energy Procedia 51, 253–258.

Sannan, S., Kerstein, A. R., 2016. Differential molecular diffusion in a hydrogen-rich jet. Energy Procedia 86, 304–314.

Sannan, S., Weydahl, T., Kerstein, A. R., 2013. Stochastic simulation of scalar mixing capturing unsteadiness and small-scale structure based on mean-flow properties. Flow, Turbulence and Combustion 90, 189–216.

Schmidt, R. C., Kerstein, A. R., McDermott, R., 2010. ODTLES: A multi-scale model for 3D turbulent flow based on one-dimensional turbulence modeling. Comput. Methods Appl. Mech. Eng. 199 (13-16), 865–890.

Sen, B. A., Menon, S., 2010. Linear eddy mixing based tabulation and artificial neural networks for large eddy simulations of turbulent flames. Combustion and Flame 157, 62–74.

Smith, G. P., Golden, D. M., Frenklach, M., Moriarty, N. W., Eiteneer, B., Goldenberg, M., Bowman, T. C., Hanson, R. K., Song, S., Gardiner, W. C. J., Lissianski, V. V., Qin, Z., 1999. GRIMech30. http://www.me.berkeley.edu/gri_mech/.

This is the accepted version of an article published in Combustion Science and Technology
http://dx.doi.org/10.1080/00102202.2019.1588261

Ströhle, J., Myhrvold, T., 2007. An evaluation of detailed reaction mechanisms for hydrogen combustion under gas turbine conditions. International Journal of Hydrogen Energy 32 (1), 125–135.

Sun, H., Yang, S., Jomaas, G., Law, C., 2007. High-pressure laminar flame speeds and kinetic modeling of carbon monoxide/hydrogen combustion. Proceedings of the Combustion Institute 31 (1), 439–446.

Tennekes, H., Lumley, J. L., 1972. A First Course in Turbulence. MIT press.

Weydahl, T., 2010. A Framework for Mixing-Reaction Closure with the Linear Eddy Model. Ph.D. thesis, NTNU Trondheim.

Yoo, C. S., Chen, J. H., Sankaran, R., 2007. A 3D DNS study of the stabilization of a turbulent lifted hydrogen/air jet flame in an autoignitive heated coflow. In: 2007 Fall Meeting of the Western States of the Combustion Institute. Paper # 07F57.

Yoo, C. S., Sankaran, R., Chen, J. H., 2009. Three-dimensional direct numerical simulation of a turbulent lifted hydrogen jet flame in heated coflow: flame stabilization and structure. Journal of Fluid Mechanics 640, 453–481.

Zsély, I. G., Zádor, J., Turányi, T., 2005. Uncertainty analysis of updated hydrogen and carbon monoxide oxidation mechanisms. Proceedings of the Combustion Institute 30 (1), 1273–1281.

Zuse, K., 1972. Der Plankalkül. Berichte der Gesellschaft für Mathematick und Datenverarbeitung. BMBW-GMD-63, 235–285.

This is the accepted version of an article published in Combustion Science and Technology
http://dx.doi.org/10.1080/00102202.2019.1588261

Nomenclature

Greek Symbols

η	Kolmogorov length scale $= (\nu_M/\varepsilon)^{1/4}$ [m]
ν_M	Molecular kinematic viscosity [m^2/s]
ν_T	Turbulent kinematic viscosity [m^2/s]
ω_k	Chemical reaction rate [$(kg)_k/kg/s$]
ρ	Density [kg/m^3]
σ_T	Turbulent Schmidt number $=\nu_T/D_T$
σ_h	Turbulent Prandtl number of the energy equation
σ_{Y_i}	Turbulent Schmidt numbers of the mass balance equations
ε	Dissipation term in the equation for turbulence energy [m^2/s^3]

Superscripts

$-$	Mean value
$\sim$	Mass-weighted average value
”	Fluctuating value

Latin Symbols

Δt	RANS time step [s]
Δx	RANS cell size [m]
Δx_w	LEM cell size [m]
ξ	Mixture fraction
C_μ	Constant in the k-ε model
D_k	Molecular diffusivity [m^2/s]
D_T	Turbulent diffusivity [m^2/s]
k	Turbulent kinetic energy [m^2/s^2]
L_{int}	Integral length scale [m]
p	Scaling exponent in the Linear Eddy Model
t	Time [s]
TM	Triplet Map
u	Fluid velocity [m/s]
W	Molecular weight [g/mol]
X_k	Mole fraction of species k $[(mol)_k/mol]$
Y_k	Mass fraction of species k $[(kg)_k/kg]$
Z	Elemental mass fractions
fac	Under-resolving factor $= \Delta x_w/\eta$
p	Static pressure [Pa=N/m^2]

Aberrations

3DCV	Control volume in LEM3D
CFD	Computational fluid dynamics
CFL	Advective Courant-Friedrichs-Lewy number
CV	Control volume
DNS	Direct Numerical Simulation
LEM	The standalone Linear Eddy Model
LEM_{res}	# of LEM wafers in each direction of the 3DCVs
LEM3D	The three-dimensional Linear Eddy Model formulation
LES	Large Eddy Simulation
RANS	Reynolds Averaged Navier-Stokes equations

This is the accepted version of an article published in Combustion Science and Technology
http://dx.doi.org/10.1080/00102202.2019.1588261

Table 1: Numerical conditions for the RANS computations of the cold-flow jet and the lifted flame in a vitiated co-flow.

RANS domain	Cuboid, $75 \times 75 \times 60$
Solver	Steady state
Turbulence model	Modified κ-ε with $C_\mu = 0.09$ $C_{1\varepsilon} = 1.44$ $C_{2\varepsilon} = 1.83$ $\sigma_k = 1$ $\sigma_\varepsilon = 1.3$ $\sigma_h = 0.7$ $\sigma_{Y_i} = 0.6$
Turbulence-Chemistry Interaction:	Eddy Dissipation Concept
Discretization schemes	Standard for pressure SIMPLEC for pressure-velocity coupling Second order upwind for momentum and turbulent kinetic energy
Under-relaxation factors	Pressure= 0.3 Body forces= 0.9 Density= 0.9 Momentum= 0.7

Table 2: Flame and flow boundary conditions of the jet flame and the co-flow.

	Central jet	Co-flow
Volumetric flow of H_2 [L_{STP}/min]	25	225
Volumetric flow of N_2 [L_{STP}/min]	75	
Volumetric flow of air [L_{STP}/min]		2100
Temperature [K]	305	1045
Mean velocity [m/s]	107	3.5
Reynolds number	23600	18600
Diameter [m]	0.00457	0.21
Mean mole fraction, H_2	0.2537	0.0005
Mean mole fraction, N_2	0.7427	0.7532
Mean mole fraction, O_2	0.0021	0.1474
Mean mole fraction, H_2O	0.0015	0.0989

This is the accepted version of an article published in Combustion Science and Technology
http://dx.doi.org/10.1080/00102202.2019.1588261